Electronic Supplementary Information (ESI) for

Quantitative electrical homogeneity assessment of nanowire transparent electrodes

DOI: 10.1039/d2nr06564a

Davide Grazioli[a,*], Alberto C. Dadduzio[a], Martina Roso[a], Angelo Simone[a]

[a] *Department of Industrial Engineering, University of Padova, Padua, Italy*

S1. Methods

S1.1. Observable geometry: Numerical sample generation

We generate two-dimensional numerical samples using a Monte Carlo procedure. Each realization, denoted as 'observable geometry', is defined in a $L \times L$ domain containing nanowires (NWs) of length l_w represented as widthless sticks (*i.e.*, line segments). Sticks are free to intersect and are placed in the domain with no preferential orientation (random arrangement). The middle point coordinates and orientation angle of each stick are extracted from a uniform probability distribution. During the generation of the observable geometry, portions of segments intersecting the domain edges are cut at the intersection point and moved to the opposite edge, resulting in a periodic arrangement of segments (Fig. 1a). The stick density n (eqn (1)) quantifies the number of NWs N_w contained in the observable geometry.

S1.2. Percolation network

A percolation detection procedure is performed on each observable geometry. To determine if an observable geometry is percolated, contacting sticks are grouped into clusters [1]. A cluster is a collection of contacting sticks. Two sticks are in contact if they intersect. An observable geometry is percolated if a 'percolating cluster' is detected (a percolating cluster is therefore a cluster spanning across two opposite edges of the numerical sample). The 'percolation network' is the union of 'percolating clusters', should they exist. The percolation network (Fig. 1b) is a subset of the sticks of the observable geometry.

S1.3. Electrical response evaluation

The percolation network is converted into an equivalent resistor network to determine the corresponding electric current intensity map (Fig. 1c) and effective current I_{eff}. Stick segments not belonging to the percolation network do not

*Corresponding author
Email addresses: davide.grazioli@unipd.it (Davide Grazioli), albertocarmine.dadduzio@unipd.it (Alberto C. Dadduzio), martina.roso@unipd.it (Martina Roso), angelo.simone@unipd.it (Angelo Simone)
ORCID iDs: https://orcid.org/0000-0003-2495-1508 (Davide Grazioli), https://orcid.org/0000-0002-6528-0432 (Alberto C. Dadduzio), https://orcid.org/0000-0001-6430-2751 (Martina Roso), https://orcid.org/0000-0001-9726-0068 (Angelo Simone)

contribute to the conduction process and are merely disregarded. For the purpose of electrical conduction evaluation only, NWs are regarded as right circular cylinders of diameter d_w. The NW resistance is calculated as $R_w = l_w/(\kappa_w A_w)$, where κ_w is the material conductivity and $A_w = \pi d_w^2/4$ is the cross-sectional area of the NW. The value of d_w is not considered for the areal coverage computation and affects subsequent evaluations exclusively through R_w.

The resistor network is defined through nodes and resistor elements. Nodes are generated at i) intersection points between sticks and edges of the domain, and ii) intersection points between two sticks. In the first case, a single node is created at each intersection. Boundary conditions are applied at nodes on the edges of the domain (representing NWs in contact with external electrodes [2, 3]). In the second case, a couple of nodes with the same spatial coordinates is introduced and each node is associated to either one of the intersecting sticks (duplicated-node approach). A contact resistor element with resistance R_j connects the couple of nodes. Stick segment resistor elements of resistance $R_s = l_s/l_w\, R_w$ connect adjacent nodes on a stick, being l_s distance between adjacent nodes along the stick. We assign the same value of R_j to all contact elements. Although the duplicated-node approach allows to address all possible resistance scenarios ranging from stick-dominated to junction-dominated, its use is not recommended when $R_w \gg R_j$. Numerical simulations concerning scenario $R_w \gg R_j$ are performed generating a single node at the intersection between sticks (single-node approach). Since the node is shared by the two intersecting sticks, the single-node approach is equivalent to the duplicated-node approach with $R_j = 0$ but is numerically more robust. In summary, two equivalent resistor networks are generated from each percolated network using different approaches: the duplicated-node approach and the single-node approach. The former is used when $R_w = R_j$ and $R_w \ll R_j$, the latter when $R_w \gg R_j$. Contact resistors elements are not introduced at the intersection between stick and edges in any case. The stick segments of the original geometry are reduced to sub-segments at this stage (Fig. 1c). The values of κ_w and R_j are duly selected to meet the conditions representing each of the three resistance scenarios in the numerical simulations (refer to Table S2 for details).

Application of Kirchhoff's laws to the elements in the network leads to a system of linear equations [4] which is obtained by using standard Finite Element Method procedures [5]. The element resistance R_e is equal to R_j and R_s for contact and segment resistor elements, respectively. A potential difference ΔV is applied between nodes that belong to a pair of opposite edges of the domain (Dirichlet boundary condition), while the electric current is set to zero (Neumann boundary condition) on the nodes lying on the edges parallel to the direction of the applied potential difference. Once the potential v is known at all nodes, the electric current I_e flowing through each e-th resistor element is computed as

$$I_e = (v_{e2} - v_{e1})/R_e,$$

being v_{e1} and v_{e2} the electric potential of the nodes identifying the e-th element. The effective current flowing through the network is

$$I_{\text{eff}} = \sum_{i}^{N_e} I_i,$$

with the sum performed on the N_e resistor elements connected to one of the edges on which the electric potential is set. We therefore evaluate the effective conductivity κ_{eff} of the electrode through eqn (2), which is suitable for an

electrode of $L \times L$ surface and unit thickness. The power and the areal power density of the electrode are computed through eqn 4 and 5, respectively.

When the percolation network is converted into an equivalent resistor network, the sticks of the percolation network are split into stick segments (to be converted into stick segment resistor elements). The 'conduction network' is identified as the current-carrying subset of the percolating network, that is, the stick segments of the percolation network that actually participate to electronic conduction. Non-conducting (dangling ends) stick segments (Fig. 1c) are identified as the stick segments for which condition $I_e < I_{\text{threshold}}$ holds, being $I_{\text{threshold}}$ a threshold value below which all currents are set to zero. We set $I_{\text{threshold}} = I_{\text{eff}} \times 10^{-6}$ for convenience.

S1.4. Areal coverage evaluation

The numerical sample is divided with a grid of $N_{\text{q}} \times N_{\text{q}}$ quadrats (Figures 1d,e,f) with edges of length $l_{\text{q}} = L/N_{\text{q}}$. The ratio between the stick length and the length of the quadrat edge (*i.e.*, $l_{\text{w}}/l_{\text{q}}$) defines the grid resolution.

The areal coverage is computed as the ratio $N_{\text{criterion}}/N_{\text{qt}}$ between the number of quadrats $N_{\text{criterion}}$ satisfying a certain criterion and the total number of quadrats $N_{\text{qt}} = N_{\text{q}}^2$. In the analysis of observable geometry (Fig. 1a) and percolation network (Fig. 1b), we count the quadrats either containing or intersected by at least a stick (Fig. 1d and Fig. 1e, respectively). In the analysis of the conduction network (Fig. 1c), we count the quadrats that either contain or are intersected by at least a resistor element e (contact or segment resistor element) such that the current flowing through the element is $I_e > I_{\text{threshold}}$ (Fig. 1f). The analysis of the spatial distribution of the areal power density is performed considering the quadrats whose areal power density $\mathcal{P}_{\text{q}}$ (eqn (6)) satisfies condition $\mathcal{P}_{\text{q}} > \alpha_{\text{factor}}\, \mathcal{P}_{\text{eff}}$. Figures 3 and 4 are obtained with $\alpha_{\text{factor}} \in [0, 3]$.

In the numerical implementation of this process, each item of the ensemble under examination (either segments representing stick or resistor elements) is converted into sub-items identified by i) the intersection points between the item and the grid, and ii) the endpoints of the item (Figs. 1d,e,f and S1). Each sub-item is assigned to the quadrat containing its midpoint. In the analysis of observable geometry, percolation network, and conducting network, a quadrat is considered in the count of $N_{\text{criterion}}$ if it contains (at least) a sub-item.

The analysis of the areal power density is a more intricate process that involves the individual elements of the resistor network. To conduct this analysis, segment resistor elements that intersect the grid lines are partitioned into smaller sub-elements. Each portion of a segment resistor element i is a sub-element of length $l_{\text{se},i}$ and power $I_i^2\, R_{\text{w}}\, l_{\text{se},i}/l_{\text{w}}$, being I_i the electric current flowing through element i. The power of a contact resistor element j is $I_j^2\, R_{\text{j}}$. The power of the quadrat P_{q} is thus

$$P_{\text{q}} = \frac{R_{\text{w}}}{l_{\text{w}}} \sum_{i}^{\text{N}_{\text{r}}} I_i^2\, l_{\text{se},i} + R_{\text{j}} \sum_{j}^{\text{N}_{\text{j}}} I_j^2, \tag{S.1}$$

that is, the sum of the power contributions of N_{r} portions of resistor segments plus N_{j} contact resistors lying in the quadrat (refer to the next section for details). The calculation of the areal power density of the quadrat (*i.e.*, $\mathcal{P}_{\text{q}} = P_{\text{q}}/l_{\text{q}}^2$) trivially follows.

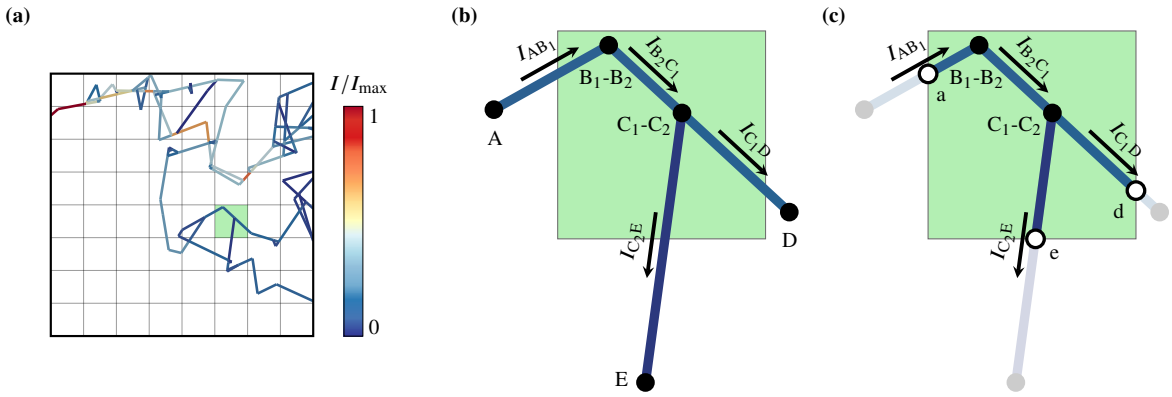

Fig. S1. Evaluation of the areal power density within a single quadrat. (a) Conduction network and electric current intensity map are overlaid onto an electrode discretization with a grid resolution $l_w/l_q = 2$ (consisting of 8×8 quadrats). The numerical sample depicted in Fig. 1 is utilized, and the selected quadrat is shaded in green. (b) Nodes (full circles) and resistor elements intersecting the selected quadrat. The current I flowing through each stick segment resistor element is labeled through the couple of nodes identifying the element. (c) Sub-elements resulting from the intersection of the resistor elements shown in panel (b) with the boundaries of the selected quadrat. The intersection points (empty circles) are labeled with small letters consistent with the labels of the nodes that identify the elements. The portions of stick resistor elements outside the quadrat are shaded in gray.

S1.5. Areal power density evaluation

The procedure is elucidated considering junction resistor elements (duplicated-node approach according to section S1.3). Figure S1a shows the conduction network extracted from the observable geometry depicted in Fig. 1a and its current intensity map. A $l_w/l_q = 2$ resolution grid is considered (8×8 quadrats).

Figure S1b shows the elements of the resistor network intersecting the quadrat selected for the description of the overall procedure. The selected quadrat is highlighted in Fig. S1a (shaded in green). Four stick segment resistor elements are identified by couples of nodes A-B_1, B_2-C_1, C_1-D, and C_2-E. Nodes B_2 and C_2 are the replicas of node B_1 and C_1, respectively. Two junction resistor elements are defined by the couple of nodes B_1-B_2 and C_1-C_2. No junction element is introduced between stick segment elements B_2-C_1 and C_1-D because they represent adjacent portions of the same stick (refer to the observable geometry of Fig. 1). Stick segment resistor elements and the current I flowing through them are labeled using the couple of nodes identifying the element.

Figure S1c shows the sub-elements resulting from the intersection of the stick segment resistor elements shown in Fig. S1b with the boundary of the selected quadrat. The intersection points are labeled with a, d, and e according to the capital letters used for the nodes and identify the elements that fall outside the selected quadrat. Expressing with $l_{B_2C_1}$ the length of element B_2C_1, and with l_{aB_1}, l_{C_1d}, and l_{C_2e} the lengths of the sub-elements, eqn (S.1) reads

$$P_q = \frac{R_w}{l_w}\left(I^2_{AB_1}\, l_{aB_1} + I^2_{B_2C_1}\, l_{B_2C_1} + I^2_{C_1D}\, l_{C_1d} + I^2_{C_2E}\, l_{C_2e}\right) + R_j\left(I^2_{AB_1} + I^2_{C_2E}\right),$$

for the selected quadrat (notice that $I_{B_2C_1} = I_{AB_1}$). We employed the efficient MATLAB implementation for segment intersection detection provided by Erdem [6].

Numerical simulations concerning scenario $R_w \gg R_j$ are performed adopting the single-node approach. In this

case, no duplicated nodes are introduced at the contact points between different sticks. Considering the example discussed so far, nodes B and C replace the couple of nodes B_1-B_2 and C_1-C_2, respectively. Adapting the notation accordingly, the equation above simplifies to

$$P_q = \frac{R_w}{l_w} \left(I_{AB}^2 \, l_{aB} + I_{BC}^2 \, l_{BC} + I_{CD}^2 \, l_{Cd} + I_{CE}^2 \, l_{Ce} \right) .$$

The areal power density of the quadrat is evaluated as $\mathcal{P}_q = P_q / l_q^2$ for both single- and duplicated-node approaches.

S2. Macroscopic characterization of nanowire electrodes

The macroscopic characterization of nanowire network electrodes (NW electrodes) is described in this section. The identification of the percolation threshold is treated first. The relationship between effective conductivity κ_{eff}, stick density n, and ratio R_w/R_j is discussed next. Even if the arguments presented in this section constitute no novelty, they are relevant for two main reasons. First, the comparison against established results allows to verify the numerical framework for i) the generation of the observable geometries, ii) their conversion into equivalent resistor networks, and iii) the computation of the electric current flowing through the network. The verification of these components of the framework is important because the overall homogeneity assessment relies on them. Second, the effective areal power density $\mathcal{P}_{eff}$ is determined through eqs 4 and 5 using effective current I_{eff} and applied potential ΔV. Since the effective current I_{eff} is trivially obtained from the effective conductivity κ_{eff} through eqn (2), the data provided in this section integrate the description of the electrical homogeneity assessment. The results are presented in terms of κ_{eff} to ease the comparison against available analytical solutions, as described in the following paragraphs. Our analysis is based on the simplifying assumption that the effective conductivity is independent of the applied potential, a condition which is not necessarily met in real electrodes as demonstrated, for example, by Sannicolo et al. [7].

The observable geometry is employed for the identification of the percolation threshold. Numerical realizations are generated according to the procedure described in section S1.1. To determine if an observable geometry forms a percolation network, the sticks are grouped into clusters [1]. Two sticks are assigned to the same cluster if they intersect. The observable geometry is percolated if at least one cluster extends between two opposite edges of the domain. The percolation network coincides with the union of the clusters extending between two opposite edges of the domain (Fig. 1). Numerical simulations are performed with domain size ranging between $L = 4l_w$ and $L = 16l_w$ according to the setting listed in Table S1. For the percolation threshold investigation, we generate 500 numerical realizations for each value of stick density (and for each domain size). The search for the percolation network is performed along x and y directions.

Figure S2a shows the cumulative percolation probability curve, *i.e.*, the probability of a specimen to be percolated versus the stick density n. The cumulative percolation probability curves obtained for the x- and y-directions (and for the same set of specimens) show no appreciable differences. We thus report the results that refer to the x-direction only. Following the approach of Finner et al. [9], we identify the percolation threshold as the value of n at the crossing point of the curves obtained with domains of different size. According to Fig. S2a, we estimate a percolation threshold $n_c = 5.64$,

Table S1. Simulation settings for the identification of the percolation threshold.

domain size	stick density range (n)
$L = 4l_w$	2 - 11[a]
$L = 8l_w$	2.5 - 9.5[a]
$L = 16l_w$	3 - 8.5[a]

[a] Numerical simulations are performed at stick density values sampled within the stick density range indicated with increment size equal to 0.5.

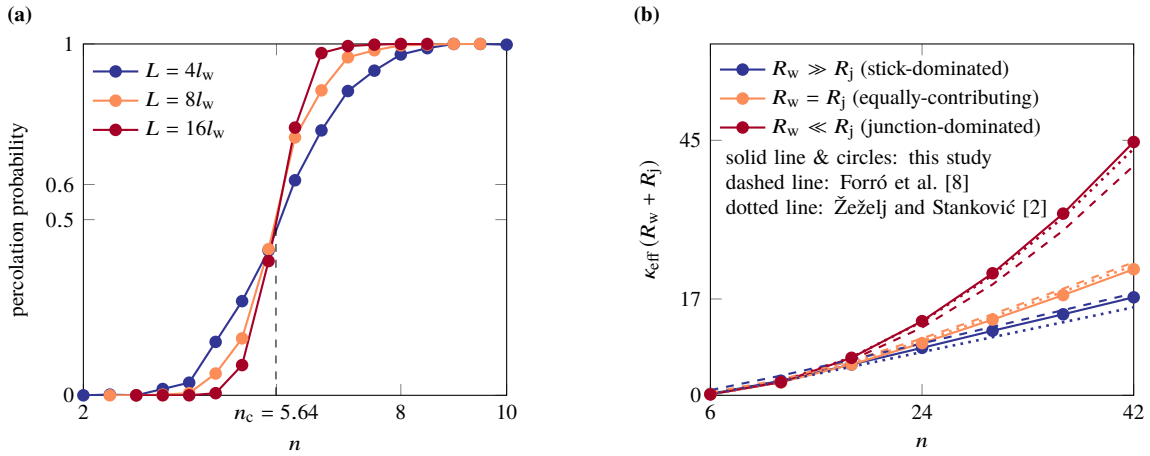

Fig. S2. Macroscopic characterization of the NW electrodes. (a) Percolation probability versus stick density for domain sizes $L = 4l_w$, $8l_w$ and $16l_w$. The percolation probability represents the proportion of percolated samples out of the 500 realizations created for each combination of domain size and stick density n. It is calculated by dividing the number of percolated samples by the total number of samples generated. The numerical simulation setting is described in Table S1. (b) Normalized conductivity $\kappa_{eff}\ \left(R_w + R_j\right)$ versus stick density for three resistance scenarios. Details about the numerical simulation settings are given in Table S2. Numerical simulations are performed with domain size $L = 4l_w$ (continuous lines and full circles). Each circle represents the average of 100 realizations. Two sets of results obtained with analytical expressions are included for reference: dashed lines represent the results obtained using the inverse of the sheet resistance obtained through eq 6 by Forró et al. [8]; dotted lines represent the results obtained through eq 7 by Žeželj and Stanković [2]. The same color is used to identify the same resistance scenario.

Table S2. Numerical simulation settings for effective conductivity identification and spatial assessment.

	resistance	parameter	symbol	value(s)
geometry		NW length[a]	l_w	35 µm
		NW diameter[a,b]	d_w	6.5×10^{-2} µm
		domain size	L	$4l_w$
		stick density	n	6 - 42[c]
boundary conditions		potential difference[d]	ΔV	1 V
material properties[b]	$R_w \gg R_j$[e] (stick-dominated)	NW conductivity	κ_w	7.032×10^6 S m^{-1}
		contact resistance	R_j	0
	$R_w = R_j$[f] (equally contributing)	NW conductivity	κ_w	7.032×10^6 S m^{-1}
		contact resistance	R_j	1500 Ω
	$R_w \ll R_j$[g] (junction-dominated)	NW conductivity	κ_w	5.0×10^{10} S m^{-1}
		contact resistance	R_j	1500 Ω
spatial assessment		grid resolution[h]	l_w/l_q	1 - 32

[a] Value selected according to Jagota and Tansu [11].
[b] We assume each NW is described as a straight right circular cylinder, of diameter d_w and electronic conductivity κ_w, and compute its resistance as $R_w = l_w/(\kappa_w A_w)$ being $A_w = \pi d_w^2/4$ the cross-sectional area of the NW.
[c] Numerical simulations are performed with stick densities sampled at n = 6, 12, 18, 24, 30, 36, and 42. The number of realizations (observable geometries) generated for each value of stick density is 100.
[d] This value is provided for completeness only. As we assume a linear response of the conduction network, the overall electrical homogeneity assessment is independent of the actual value of ΔV.
[e] Numerical simulations are performed with the single-node approach described in the section S1.3.
[f] Numerical simulations are performed with the duplicated-node approach described in section S1.3.
[g] Numerical simulations are performed with the duplicated-node approach described in section S1.3. Material properties are selected to ensure that $R_w/R_j \approx 1/7000$ in the numerical simulations. Increasing the value of κ_w while keeping R_j unchanged does not lead to appreciable differences in terms of normalized conductivity $\kappa_{eff}\,(R_w + R_j)$. The relationship between $\kappa_{eff}\,(R_w + R_j)$ and stick density n for each resistance scenario is shown in Fig. S2b.
[h] Spatial assessment is performed with grid resolutions l_w/l_q = 1, 2, 4, 8, 16, and 32.

which is in perfect agreement with the value identified by Li and Zhang [10] (they report $n_c = 5.63726$).

The percolation network is converted into an equivalent resistor network adopting the procedure described in section S1.3. We compute the effective conductivity of the electrode as $\kappa_{eff} = I_{eff}/\Delta V$ (eqn (2)), according to the definition of conductivity adopted by Žeželj and Stanković [2] (refer to footnote 30 therein). Numerical simulations are performed with the setting described in Table S2, and 100 realizations are generated for each value of stick density (and for each resistance scenario). The analysis is performed along x and y directions.

Figure S2b shows the normalized effective conductivity $\kappa_{eff}\,(R_w + R_j)$ versus stick density n for three resistance scenario: $R_w \gg R_j$ (stick-dominated), $R_w = R_j$ (equally contributing), and $R_w \ll R_j$ (junction-dominated). Each circle in the plot is the average of 100 realizations (the conductivity of non-percolated samples is considered to be equal to zero). The results of the analytical expressions derived by Forr'o et al. [8] and Žeželj and Stankovi'c [2] (shown as dashed and dotted lines, respectively) are compared with the effective conductivity. The comparison against the conductivity determined through eq 7 by Žeželj and Stanković [2] is straightforward, while Forró et al. [8] consider the sheet resistance. Notice that, according to the definition adopted in this study, the effective conductivity (eqn (2)) is equivalent to the inverse of the sheet resistance (R_{eff} according to our eqn (S.9), R_s according to Forró et al. [8]). Since our results fall within the range identified by the two analytical solutions (the relative difference between our results and each analytical solution is 11% at the most), we conclude that our numerical framework for the

effective conductivity evaluation is verified. We observe that, analogously to the percolation threshold, the effective conductivity cannot be distinguished when evaluated either in x or y direction. We thus conclude that the macroscopic response of the generated samples is, on average, isotropic.

The size of the numerical simulation domain is known to affect the prediction of NW electrode properties (refer, for example, to Žeželj and Stanković [2] and Li and Zhang [10]). This aspect also emerges from Fig. S2a, where the insulator-to-conductor transitions becomes sharper as the domain size L/l_w increases. Han et al. [12] perform a numerical investigation to identify the size of the representative volume element (RVE) for two-dimensional nanowire electrode simulations. That is, the smallest domain size whose effective properties represent (with a certain accuracy) the macroscopic response of the electrode. Han et al. [12] conclude that RVEs of size L/l_w ranging between 50 and 100 are best suited for the evaluation of the electrode effective properties at $n \approx n_c$; however, 'far from the percolation threshold' (they consider nanowire content equivalent to $n = 5n_c$ at the most) a simulation domain of size L/l_w ranging between 3 and 6 is appropriate. The results by Han et al. [12] (their Figs. 7 and 8) show that at $n \approx 2n_c$ the effective properties are basically equivalent to the actual macroscopic properties if the simulation domain size is $L \geq 4l_w$ (if the aspect ratio of the NWs is $l_w/d_w \geq 100$). All the numerical results of this contribution are obtained with a domain size $L = 4l_w$ (the percolation threshold investigation represents the only exception). The selection of the domain size was based on a trade-off between computational cost and accuracy and taking into account prior research. Jagota and Tansu [11], for example, perform a numerical investigation about the relationship between stick orientation and effective conductivity. They also employ two-dimensional domains of size $L = 4l_w$. Kim and Nam [13] perform a numerical investigation on the conductivity of silver nanowire (AgNW) networks making use of digital domains of size L ranging between 5 l_w and 15 l_w. In the same contribution, the size of the simulation domains is reduced to $L = 3l_w$ when the numerical model is compared against experimental observations. Kim and Nam [14] also show that numerical estimates of the electrical conductivity obtained with digital domains of size between $L = 5l_w$ and $15l_w$ are similar. Langley et al. [15] show that a domain of size $L \approx 4l_w$ leads to a perfect agreement between theoretically estimated resistance and experimentally measured resistance for AgNW networks employed in solar cell applications (Fig. 6a in [15]). Furthermore, Fig. S2b shows the effective conductivity computed with the analytical solution by Žeželj and Stanković [2] (with $L/l_w = 4$), and we observe no appreciable difference by performing the calculations with $L/l_w > 4$. These considerations suggest that a domain size $L = 4l_w$ is a reasonable choice. A domain of size $L = 4\,l_w$ is also consistent with experimentally available data by Sannicolo et al. [7] (refer to the validation procedure described in sections 2.3 and S5). A few extra comments about it are given in the following sections.

S3. Areal coverage of the observable geometry: Analytical prediction

The areal coverage of the original geometry (Fig. 1) is related to the transparency of the electrode. Tarasevich et al. [3] investigate the relationship between the number of sticks ('zero-width rods' in the reference) per unit area and the transmittance of two-dimensional films with an approach analogous to the one described in section 2.2. They generate two-dimensional realizations by distributing sticks randomly and uniformly over a square domain of size L. The domain is then divided into $N_q \times N_q$ square cells of equal size $l_q = L/N_q$, and cells that contain at least a (portion

of a) stick are considered 'opaque' (they are considered transparent otherwise).

Tarasevich et al. [3] compute the transmittance of the film as

$$T = 1 - p, \tag{S.2}$$

where p is the fraction of opaque cells, and they propose the analytical expression given by

$$T = \left(1 - \frac{1}{N_\mathrm{q}^2} - \alpha_\mathrm{T} \frac{l_\mathrm{w}}{L} \frac{1}{N_\mathrm{q}}\right)^{N_\mathrm{w}} \tag{S.3}$$

to express the dependence of transmittance on stick length l_w, domain size L, number of sticks N_w, and number of quadrats N_q, with $\alpha_\mathrm{T} = 4/\pi$ for a distribution of randomly oriented sticks. Since the fraction of opaque cells p is exactly equivalent to the areal coverage C (eqn (3)) of the observable geometry, we make use of the analytical expression identified by Tarasevich et al. [3] for the verification of our numerical framework. Substitution of eqn (S.3) into eqn (S.2) while accounting for relationships $n = N_\mathrm{w}\, l_\mathrm{w}^2/L^2$ and $l_\mathrm{q} = L/N_\mathrm{q}$ allows to express p as

$$p = 1 - \left[1 - \left(\frac{l_\mathrm{w}}{L}\right)^2 \left(\frac{l_\mathrm{q}}{l_\mathrm{w}}\right)^2 - \alpha_\mathrm{T} \left(\frac{l_\mathrm{w}}{L}\right)^2 \frac{l_\mathrm{q}}{l_\mathrm{w}}\right]^{n \left(\frac{L}{l_\mathrm{w}}\right)^2}. \tag{S.4}$$

Figure 2a shows the results of eqn (S.4) for $L/l_\mathrm{w} = 4$ and for stick density n ranging from 6 to 42 and grid resolution $l_\mathrm{w}/l_\mathrm{q}$ ranging between 1 to 32. Figure 2a shows that the areal coverage of reference C_ref determined with our numerical framework perfectly agrees with the results of eqn (S.4), thus providing a verification of our numerical implementation.

S4. Homogeneity index: Evaluation details

The electrical homogeneity of the electrode is assessed through the homogeneity index $\mathcal{H}$. This scalar quantifies the extent of the deviation of the response of the electrode from the homogeneous reference response.

For a given value of the stick density n, we compute the areal coverage for different values of areal power density threshold and grid resolution. We sample C/C_ref on a two-dimensional mesh resulting from combinations of values of $\mathcal{P}_\mathrm{q}/\mathcal{P}_\mathrm{eff}$ in $[0, 3]$ at spacing 0.1 (spacing is set to 0.2 for the experimentally obtained geometries) and values of $\log_2(l_\mathrm{w}/l_\mathrm{q})$ in $[0, 5]$ with spacing 1. The contour maps in Figs. 3, 4, S5, and S6 show the result of the sampling for a selection of stick densities.

We convert the discrete collection of values into a continuous function through linear interpolation. The values of the areal coverage define a surface over the bi-dimensional domain $\left(\mathcal{P}_\mathrm{q}/\mathcal{P}_\mathrm{eff},\, \log_2(l_\mathrm{w}/l_\mathrm{q})\right) \in [0, 3] \times [0, 5]$. Considering $\log_2(l_\mathrm{w}/l_\mathrm{q})$ in place of $l_\mathrm{w}/l_\mathrm{q}$ we ensure that C/C_ref evaluated for different values of grid resolutions $l_\mathrm{w}/l_\mathrm{q}$ equally contribute to the resulting homogeneity index. Values of C/C_ref obtained at higher resolution would be more influential otherwise. The surface is described through a function f_C such that

$$f_\mathrm{C}(s, t) \in [0, 1], \quad \forall (s, t) \in [0, 3] \times [0, 5],$$

where variables s and t are used in place of $\mathcal{P}_{\mathrm{q}}/\mathcal{P}_{\mathrm{eff}}$ and $\log_2(l_{\mathrm{w}}/l_{\mathrm{q}})$, respectively. The shape of the surface is representative of the response of the system.

According to eqn (8) the surface describing the homogeneous response is

$$f_{\mathrm{C,\,homog}}\,(s,t) = \begin{cases} 1, & \text{if } s < 1,\ \forall t \in [0,5], \text{and} \\ 0, & \text{if } s \geq 1,\ \forall t \in [0,5], \end{cases}$$

and the integral over the range of values explored is

$$\mathrm{I}_{\mathrm{homog}} = \int_0^5 \int_0^3 f_{\mathrm{C,\,homog}}\,(s,t)\ \mathrm{d}s\,\mathrm{d}t = 5. \tag{S.5}$$

We thus evaluate the deviation of the electrode response from the homogeneous response as

$$\mathcal{H} = \frac{1}{\mathrm{I}_{\mathrm{homog}}} \int_0^5 \int_0^3 \left| f_{\mathrm{C}}\,(s,t) - f_{\mathrm{C,\,homog}}\,(s,t) \right|\ \mathrm{d}s\,\mathrm{d}t. \tag{S.6}$$

The (equivalent) form

$$\mathcal{H} = \frac{1}{\mathrm{I}_{\mathrm{homog}}} \int_0^5 \int_0^1 |f_{\mathrm{C}}\,(s,t) - 1|\ \mathrm{d}s\,\mathrm{d}t + \frac{1}{\mathrm{I}_{\mathrm{homog}}} \int_0^5 \int_1^3 |f_{\mathrm{C}}\,(s,t)|\ \mathrm{d}s\,\mathrm{d}t \tag{S.7}$$

is more convenient if numerical integration is performed, which is the case here.

Notice that the actual value of $\mathcal{H}$ depends on factors such as the range of values $\left(\mathcal{P}_{\mathrm{q}}/\mathcal{P}_{\mathrm{eff}},\ \log_2(l_{\mathrm{w}}/l_{\mathrm{q}})\right)$ explored and the sampling intervals. Relative comparison (*e.g.*, trend of $\mathcal{H}$ versus n for different values of ratio $R_{\mathrm{w}}/R_{\mathrm{j}}$) are thus more informative than the mere value of $\mathcal{H}$.

S5. Experimental samples: Digitization and macroscopic characterization

We describe the numerical analysis performed on the experimentally obtained NW geometries [7] shown in Fig. 4a. Each scanning electron microscopy (SEM) image shows a distribution of silver nanowires (AgNWs) and covers an area of about 25 μm $\times$ 21.5 μm. After digitization, the AgNWs distributions are examined with the strategy proposed in this work. A characterization of the digitized geometries is also performed and effective properties are determined. The results are discussed by making reference to the characterization performed by Sannicolo et al. [7], which is based on specimens with size 25 mm $\times$ 25 mm ('entire sample' from now on) from which the SEM images were extracted.

S5.1. Experimental samples: Digitization

Sannicolo et al. [7] obtained the electrical potential distribution of AgNWs electrodes by scanning 25 mm $\times$ 25 mm specimens at 1 mm resolution through one-probe electrical mapping. Scanning electron microscope (SEM) images of the specimens analyzed by Sannicolo et al [7] are reported in Figs. 4a and S3a for three different NW volume fractions.

The digital replicas of the NWs are superimposed to the SEM images in Fig. S3a. We represent NWs as sticks. For the detection of the percolation network, we consider two NWs connected if the corresponding sticks intersect. To

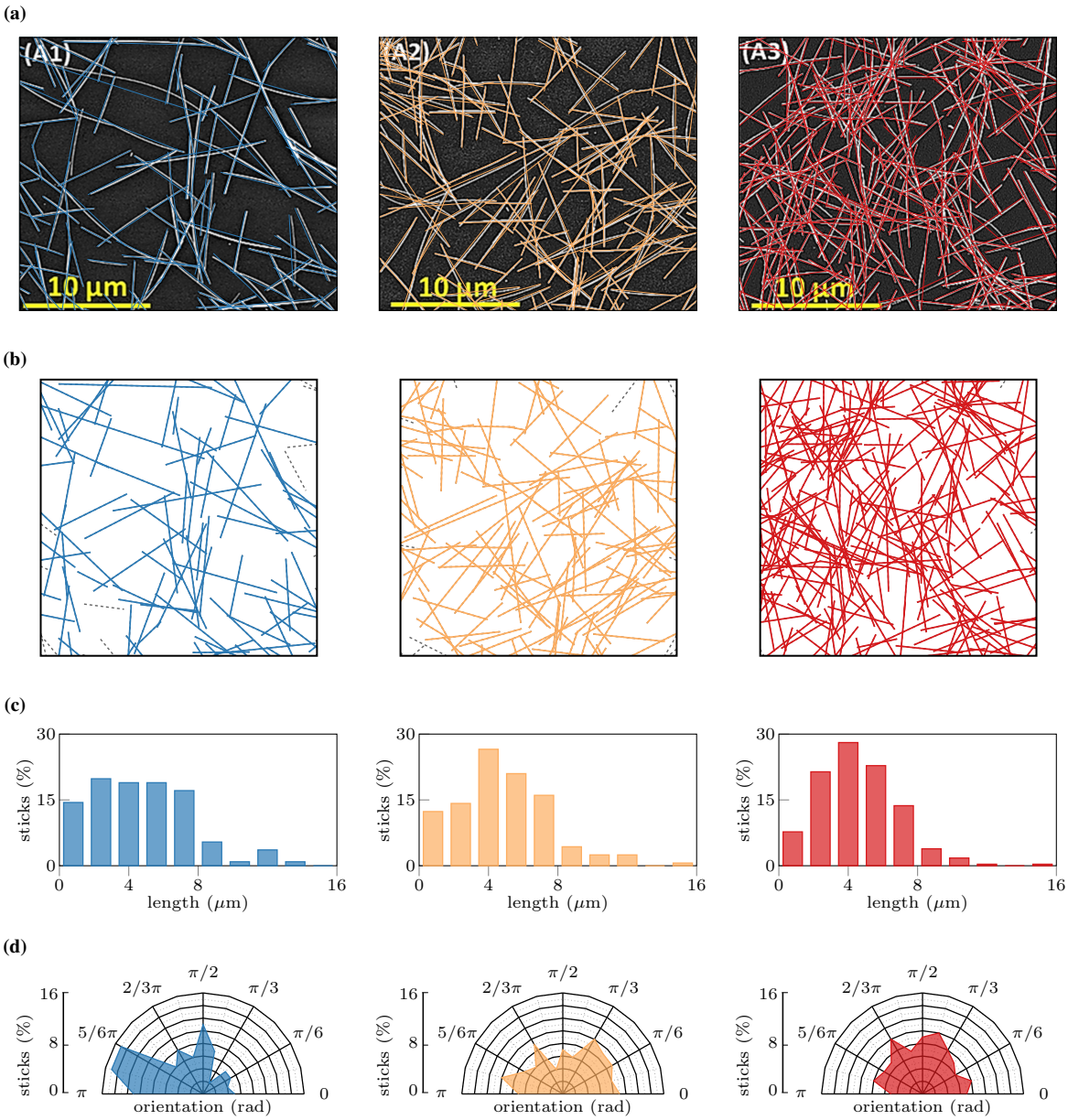

Fig. S3. Experimental samples: digitization and characterization. (a) SEM images of AgNW ensembles from Sannicolo et al. [7] (the same as in Fig. 4a). Digital replicas made of sticks are superimposed to the original images (adapted with permission from Sannicolo et al. [7]; copyright © 2018 American Chemical Society). (b) Square subsets of digital replicas shown in panel (a). Sticks of the percolation cluster are represented with colored continuous line, sticks disconnected from the percolation cluster are represented with gray dashed lines. The percolation clusters in x- and y-directions coincide for each geometry. (c) Stick length distribution. Average length l_{avg} are listed in Table S3. (d) Sticks orientation distribution. Data in panels (c) and (d) refer to all the sticks in panel (b). Additional properties are listed in Table S3.

Table S3. Characterization of experimental samples from Sannicolo et al. [7].

reference	property	geometry	sample A1	sample A2	sample A3
Sannicolo et al. [7]	AMD (mg m^{-2})	whole specimen[a]	50 ± 4	63 ± 7	86 ± 7
	sheet resistance (Ω)	whole specimen[a]	68000	329	26
this study	AMD (mg m^{-2})[b]	Fig. S3a[c]	57	90	143
		Fig. S3b[d]	57	90	146
	l_{avg} (μm)	Fig. S3a[c]	4.99	5.14	4.79
		Fig. S3b[d]	4.78	4.81	4.58
	sheet resistance (Ω)[e]	x-direction Fig. S3b[d]	189	139	73
		y-direction Fig. S3b[d]	418	115	56

[a] The values refer to the 25 mm × 25 mm specimens analyzed by Sannicolo et al. [7]. SEM images in Figs. 4a and S3a are 25 μm × 21.5 μm subsets of those specimens.
[b] Computed through eqn (S.8).
[c] Analysis performed on digital replicas superimposed to the SEM images shown in Fig. S3a.
[d] Analysis performed on geometries shown in Fig. S3b (square subsets of digital replicas in Fig. S3a). The number of sticks in the geometries is 111 (A1), 162 (A2), and 285 (A3).
[e] Sheet resistance computed through eqn (S.9). Numerical simulations performed assuming NW diameter d_w = 79 nm (average value from Sannicolo et al. [7]), bulk conductivity $\kappa_w = 63 \times 10^6$ S m^{-1}, and contact resistance $R_j = 500\,\Omega$. The values of κ_w and R_j are selected according to material parameters from Forró et al. [8] for AgNWs with diameter (approximately) equal to 80 nm (their Fig. 3h). The ratio R_w/R_j is equal to 3.096×10^{-2} (A1), 3.113×10^{-2} (A2), and 2.968×10^{-2} (A3).

ease the comparison against the specimen description provided by Sannicolo et al. [7] we express the NW content in terms of areal mass density

$$\mathrm{AMD} = \frac{\rho_{Ag}\, A_{NW}}{A_{sample}} \sum_i l_{NW,i}, \tag{S.8}$$

where we assume that NWs are right circular cylinders of diameter d_{NW}. In the expression above, ρ_{Ag} = 10.50 g cm^{-3} [16] is the density of silver, $A_{sample} \approx 534\ \mu m^2$ is the area of the sample (from the scale bar in the original images, Figs. 4a and S3a), and $l_{NW,i}$ is the length of the i-th stick in Fig. S3a. The NW cross sectional area is $A_{NW} = \pi d_{NW}^2/4$, where d_{NW} = 79 nm is the average NW diameter reported by Sannicolo et al. [7].

Table S3 lists AMD values computed with eqn (S.8) for the digitized geometries shown in Fig. S3a as well as AMD values determined by Sannicolo et al. [7]. Note that the SEM images shown in Figs. 4a and S3a represent subsets (25 μm × 21.5 μm size) of the entire samples experimentally characterized. The AMD values computed in this work exceed those found in Sannicolo et al. [7] irrespective of the sample (Table S3). Although modest for sample A1, the difference is significant for samples A2 and A3 (up to 66% relative difference). Since the digital replicas shown in Fig. S3a and the SEM images from Sannicolo et al. [7] show modest differences despite the straight sticks approximation, we conclude that the microstructures in the SEM images are not strictly representative of the entire samples analyzed by Sannicolo et al. [7]. This conclusion is supported by the fact that we identify an average length of the sticks lower than that reported by Sannicolo et al. [7] (Table S3). We find that the average stick length l_{avg} is about 5 μm (refer to Table S3), while Sannicolo et al. [7] report an average NW length of 7 ± 3 μm. The representativeness of the SEM images is further discussed at the end of this section.

Although spatial analyses based on grid discretization are suitable for rectangular domains, we chose to operate on square domains to ensure a direct comparison with the results of the spatial analyses performed on numerically

generated samples (Figs. 2 and 3). Figure S3b shows the square subsets extracted from the geometries shown in Fig. S3a. The square subsets (Fig. S3b) are obtained by virtually scanning the geometries shown in Fig. S3a with a square window (with edge equal to the height of the original geometry) and identifying the subset that minimizes the areal mass density. We obtain square subsets with stick distributions (Figs. S3c,d) perfectly consistent with those of the original geometries (not reported for brevity). AMD values are consistent with those obtained from the geometries in Fig. S3a (values reported in Table S3), and similar arguments apply to the average stick length l_{avg} (also reported in Table S3).

To draw a parallel with the results shown in Fig. 2, we analyze the NW content and the number of NWs/sticks in the domain. Assuming NWs are made of silver, an ensemble of 96 NWs of equal length $l_{\mathrm{w}} = 4.7$ μm and diameter $d_{\mathrm{w}} =$ 79 nm in a square domain of size $L = 4\,l_{\mathrm{w}}$ results in a stick density $n = 6$ (according to eqn (1)) and an areal mass density AMD $= 65.641$ mg m^{-2}. Similarly, 288 NWs result in a stick density $n = 18$ and an areal mass density AMD = 196.92 mg m^{-2}. The values of AMD and the number of sticks just reported fall in the range listed in Table S3 for the digital replicas of the SEM images and for the square subsets. It is thus reasonable to compare the spatial assessment results pertaining to the square subsets with those obtained with the numerically generated geometries at stick density n between 6 and 18 (between n_{c} and $3\,n_{\mathrm{c}}$).

The stick ensembles shown in Fig. S3b are analyzed following the procedure described in Fig. 1. First, the percolation network is extracted (Fig. 1b). The sticks that belong to the percolation network are represented with colored continuous lines in Fig. S3b, while sticks of the reference geometry not connected to the percolation network are represented by gray dashed lines. The percolation networks in x- and y-directions coincide for all the samples. Second, the percolation network is converted into an equivalent resistor network. Third, numerical simulations are performed on the equivalent resistor network to obtain the effective conductivity in x- and y-directions as well as the electric current intensity map (Fig. 1c). The resistance of each i-th stick representing a NW of length $l_{\mathrm{NW},i}$ is computed assuming that NWs are right circular cylinders of constant diameter d_{NW}. The resistance of the i-th stick resistor elements is thus

$$R_{\mathrm{w},i} = \frac{1}{\kappa_{\mathrm{w}}} \frac{l_{\mathrm{w},i}}{A_{\mathrm{w}}},$$

with $A_{\mathrm{w}} = \pi d_{\mathrm{w}}^2/4$. We assume that the value of R_{j} is the same for all contacts. Fourth, domain discretization and spatial analyses are performed following the procedure described in Figs. 1d,e,f,g.

We complete the characterization of the electrode by performing numerical simulations on the equivalent resistor networks obtained from the geometries shown in Fig. S3b. We make use of material properties available from the literature [8] (listed in Table S3) since Sannicolo et al. [7] do not report material properties, such as κ_{w}, R_{w}, or R_{j}, for their AgNW networks. Results are listed in Table S3 in terms of sheet resistance defined as

$$R_{\mathrm{eff}} = \frac{\Delta V}{I_{\mathrm{eff}}} \tag{S.9}$$

to ease comparison against the results by Sannicolo et al. [7], also reported therein.

The results of the numerical simulations clearly indicate that i) sheet resistance is inversely proportional to areal

mass density (R_{eff} progressively decreases from sample A1 to sample A3), and ii) all the samples show an anisotropic response (the sheet resistance along x- and y-directions differ).

The latter observation is consistent with the stick orientation distribution shown in Fig. S3c. The difference between sheet resistance in x- and y-directions is especially pronounced for sample A1 for which the value in the y-direction is more than double the value in the x-direction (this is due to the preferential orientation of the sticks along the x-direction, which is evident from Fig. S3c).

The differences between the values computed in this work and those experimentally obtained by Sannicolo et al. [7] are evident. The largest difference in sheet resistance concerns sample A1. The experimental measurement is 68 kΩ, while the numerical simulations lead to 418 Ω at the most. A possible reason is that the NW content of sample A1 is close to the percolation threshold. When the percolation threshold is approached, small fluctuations of NW content are known to result in a wide fluctuations of sheet resistance [17]. Indeed, Sannicolo et al. [7] highlight that "disconnected areas are only possible close to the percolation threshold and disappear for denser networks" while commenting the reconstructed voltage maps on the entire samples. Sannicolo et al. [7] determine the sheet resistance considering samples covering a surface 10^6 times larger than the SEM images we are considering. Macroscopic NW density inhomogeneity are naturally considered in their experimental evaluation, but not in ours, and this is a potential source of mismatch. Furthermore, the size of the numerical domain is known to have a significant impact on the evaluation of effective properties when the percolation threshold is approached [2, 12]. Numerical simulations performed on SEM images representing larger portions of the entire samples are therefore expected to result in smaller deviation from experimental measurements. As for samples A2 and A3, the order of magnitude of the numerically determined sheet resistance matches that of the experimentally obtained values, but differences are still considerable. The adoption of (plausible) material parameters reported in the literature, instead of *ad hoc* calibrated parameters, could be an additional reason for the mismatch between numerically and experimentally obtained values. Nevertheless, the arguments just exposed further support the claim that the geometries provided by the SEM images are not sufficiently representative of the entire samples they have been extracted from. As such, effective properties of the entire sample cannot be retrieved from the mere analysis of these geometries. Larger samples would (at the very least) be needed for this purpose. A statistical analysis performed on multiple samples would also be recommended. We thus conclude that all subsequent results must be considered as merely indicative, because an exact correlation with the results obtained on the entire specimens considered by Sannicolo et al. [7] is not possible. Nevertheless, the agreement between our results and those by Sannicolo et al. [7] supports the conclusion that the proposed methodology is suitable for the analysis of the NW ensembles in the SEM images. We stress that the analysis of the electrical homogeneity for the limiting cases $R_{\text{w}} \gg R_{\text{j}}$ and $R_{\text{w}} \ll R_{\text{j}}$ allows to compensate for the lack of material parameters resulting from an *ad hoc* calibration. Indeed, the analyses described in section 2.3 and next section lead us to conclude that our electrical homogeneity assessment indicate a range of $\mathcal{H}$ values which is consistent with the assessment reported by Sannicolo et al. [7] (in terms of electrical tortuosity).

Table S4. Investigation of experimental samples from Sannicolo et al. [7]. The numerical simulations are performed assuming NW diameter $d_w = 79$ nm [7] and bulk conductivity $\kappa_w = 63 \times 10^6$ S m^{-1}. The resulting values of R_w are 15.482 Ω (A1), 15.563 Ω (A2), and 14.839 Ω (A3). The average stick length l_{avg} reported in Table S3 is used as l_w.

sample	direction	$\kappa_{eff}\ (R_w + R_j)$		
		$R_w \gg R_j$[a] (stick-dominated)	$R_w = R_j$[b] (equally contributing)	$R_w \ll R_j$[c] (junction-dominated)
A1	x	1.132	1.416	3.044
	y	1.075	1.054	1.259
A2	x	2.113	2.310	3.987
	y	2.076	2.404	5.127
A3	x	3.643	4.172	7.631
	y	4.415	5.042	10.671

[a] Numerical simulations are performed with the single-node approach described in section S1.3.
[b] Numerical simulations are performed with the duplicated-node approach described in section S1.3.
[c] Numerical simulations are performed with the duplicated-node approach described in section S1.3. The junction resistance is set to $R_j = 8 \times 10^6 \Omega$, thus giving R_w/R_j equal to 1.935×10^{-6} (A1), 1.945×10^{-6} (A2), and 1.855×10^{-6} (A3).

S5.2. Experimental samples: Spatial analysis

We perform spatial analyses analogous to those that led to the result of Figs. 2 and 3, according to the procedure described in Figs. 1d,e,f,g. We exclusively focus on the geometries shown in Fig. S3b (reference geometries of samples A1, A2, and A3 from now on), and on the networks extracted from them. For consistency with the strategy pursued in the rest of the work, we examine the response of the electrode under the two limit conditions $R_w \gg R_j$ (stick-dominated resistance) and $R_w \ll R_j$ (junction-dominated resistance), and the intermediate condition $R_w = R_j$ (equally contributing resistance). These conditions are met with the parameters reported in Table S4. The reference R_w value is computed with $l_w = l_{avg}$.

The effective conductivity (eqn (2)) is determined according to the procedure described in section S1.3 through numerical simulations performed on the equivalent resistor network. Table S4 lists the effective conductivity of each sample in x- and y-directions. The values, provided in terms of normalized conductivity $\kappa_{eff}\ (R_w + R_j)$, are consistent with those reported in Fig. S2b at $n = 6$, 12, and 18. The ratio between the conductivity values in x- and y-directions depends on the ratio R_w/R_j. More specifically, i) the difference between the two conductivity values is maximum under junction-dominated conditions ($R_w \ll R_j$), ii) the most favorable conductivity direction depends on the value of ratio R_w/R_j for an assigned geometry (refer to values for sample A2 in Table S4), and iii) the ratio between conductivities in x- and y-directions obtained with $R_w \ll R_j$ is the closest to the value reported in Table S3 (indeed, parameter values listed in Table S3 are such that $R_w/R_j \approx 10^{-2}$).

The results of the spatial analysis are reported in Figs. 4, S4, and S5. The values on the horizontal axis are rounded so that $l_{avg}/l_q = 1$ and $l_{avg}/l_q = 32$ identify 4×4 and 128×128 grids, respectively. Being the size of the domain $L \approx 21.5$ μm and the average NW length $l_{avg} \approx 4.7$ μm, a 4×4 grid actually relates to $l_{avg}/l_q = 0.9$ and a 128×128 grid to $l_{avg}/l_q = 28$. The approximation allows us to present the results with the same format as Fig. 2.

Figure S4 summarizes the results of the spatial assessment in terms of areal coverage dependence on the grid resolution l_{avg}/l_q. Figure S4a shows the areal coverage of the reference geometry for samples A1, A2, and A3. The

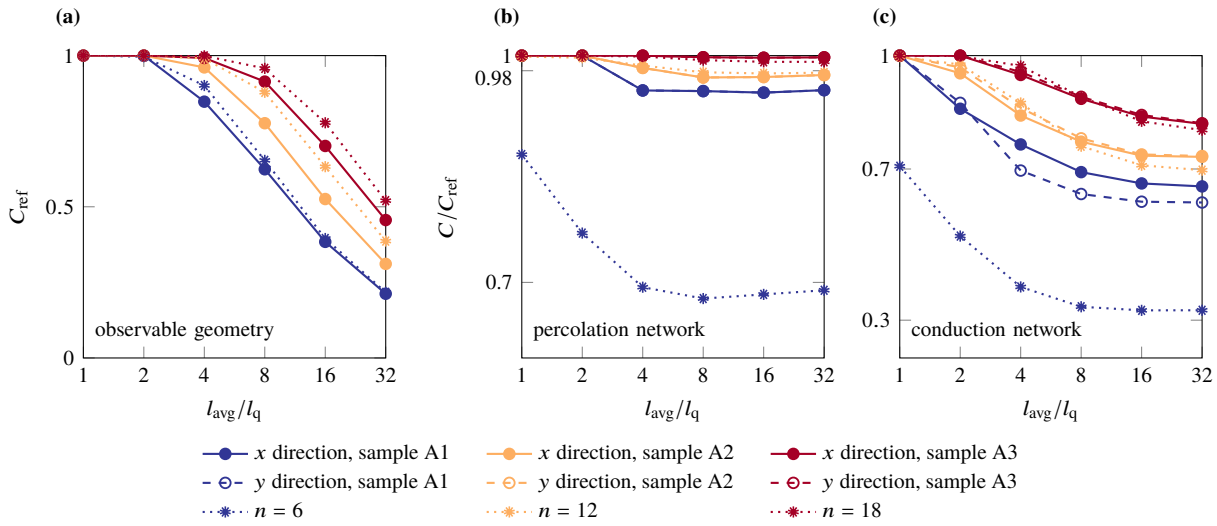

Fig. S4. Areal coverage investigation on experimental geometries. (a) Areal coverage of the observable geometries shown in Fig. S3b. (b) Areal coverage of the percolation network extracted from the observable geometries (colored sticks in Fig. S3b). (c) Areal coverage of the conduction network with perfect contact scenario ($R_w \gg R_j$). Panels (b) and (c) report results for the networks in x- (continuous line and full circles) and y- (dashed line and empty circles) directions. On the vertical axis of panels (b) and (c) the areal coverage is scaled by the areal coverage of reference C_{ref} for the same sample and grid resolution l_{avg}/l_q (panel (a)). The average values of the results obtained with numerical geometries at $n = 6$, 12, and 18 are reported for comparison (dotted lines and asterisks). Results at $n = 12$, and 18 are also reported in Figs. 2a,b,c with labels $n = 2n_c$ and $n = 3n_c$. Results at $n = 6$ are also reported in Fig. 2a with label $n = n_c$. A $\log_2$ scale representation is used for the grid resolution axis.

curves in Fig. S4a present strong analogies with those reported in Fig. 2a for $n = 6$, 12, and 18 (dotted lines with asterisks in Fig. S4). Figures S4b,c report the areal coverage for percolation and conduction networks, respectively, for x- (continuous line) and y- (dashed line) directions. A dependence of the results on the direction emerges for the conduction network only. The extent of the differences between x- and y-directions is inversely proportional to the NW content (pronounced for sample A1, modest for sample A3).

The results presented in Figs. S4b,c show analogies with the results obtained from the numerically generated geometries in Figs. 2b,c (dotted lines with asterisks in Fig. S4). Referring to the finest grid discretization ($l_{avg}/l_q = 32$ in Fig. S4, and $l_w/l_q = 32$ in Fig. 2), the values of C/C_{ref} for the percolation network are 0.954 (A1), 0.974 (A2), and 0.998 (A3) in Fig. S4b, and 0.690 ($n = 6$), 0.977 ($n = 12$), and 0.992 ($n = 18$) in Fig. 2b. For the conduction network, the values of AF/AF_{ref} are 0.654 (A1), 0.732 (A2), and 0.819 (A3) in Fig. S4c, and 0.326 ($n = 6$), 0.697 ($n = 12$), and 0.803 ($n = 18$) in Fig. 2c. The agreement between the results for samples A2 and A3 and those for $n = 12$ and $n = 18$ is noticeable. This is not the case for sample A1 and the results for $n = 6$. We believe that the close proximity of stick density $n = 6$ to the percolation threshold ($n_c = 5.64$) is the reason for the observed behavior. For this reason, a high degree of variability of the network properties (including the areal coverage of percolation and conduction networks) is expected. Since the percolation probability is about 0.6 at $n = 6$ for $L = 4l_w$, according to Fig. S2a, the existence of percolation and conduction networks is not even ensured at $n = 6$.

Figures 4 and S5 show the contour maps of the areal coverage of samples A1, A2, and A3 for varying energy

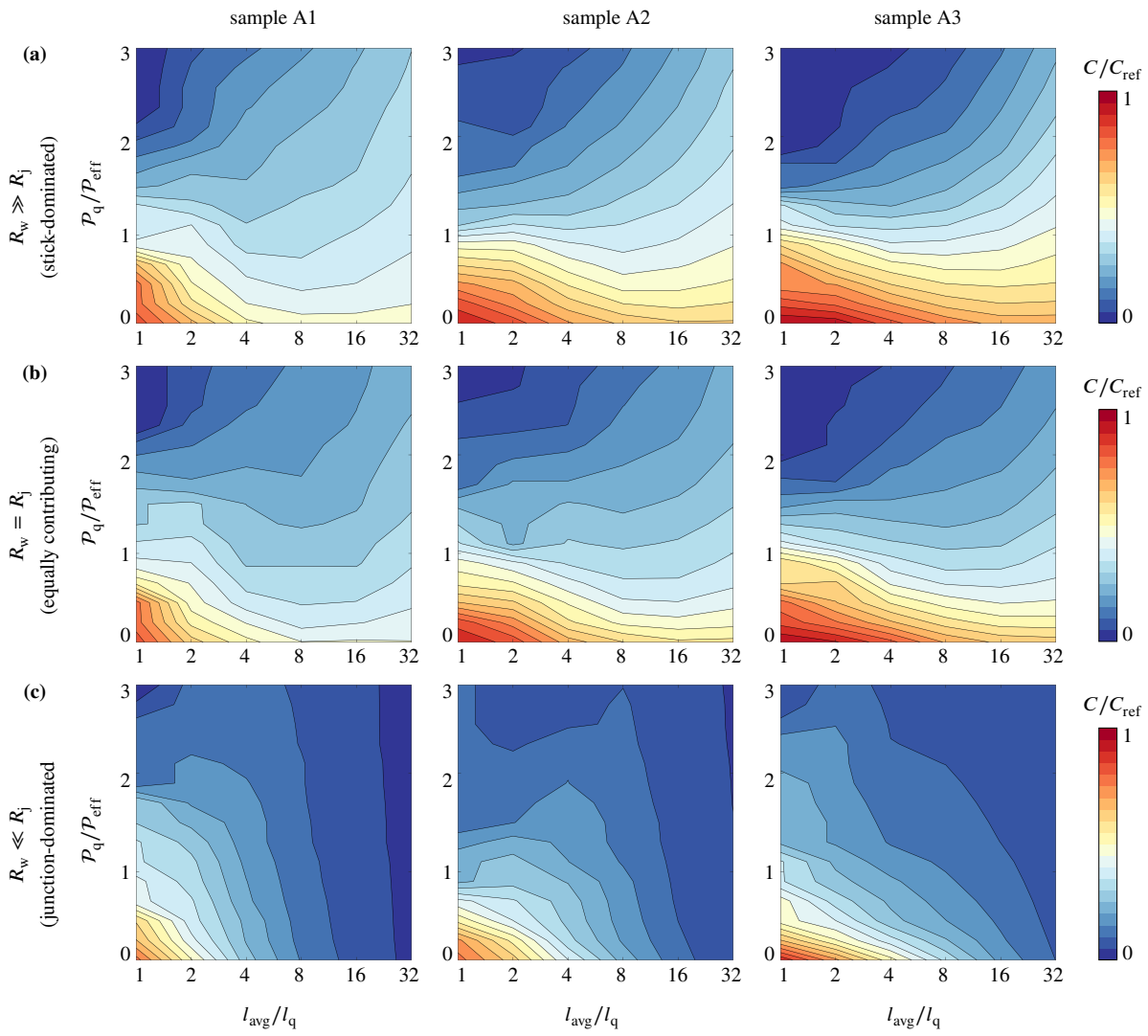

Fig. S5. Areal coverage dependence on grid resolution l_{avg}/l_q and areal power density threshold $\mathcal{P}_q/\mathcal{P}_{eff}$ for experimental geometries. Results about conduction network in the y-direction. A $\log_2$ scale representation is used for the grid resolution axis. (b,c,d) Contour maps for the digitalizations of sample A1 (left), A2 (middle), and A3 (right) as shown in Fig. S3a. Three resistance scenario are considered: $R_w \gg R_j$ (a), $R_w = R_j$ (b), and $R_w \ll R_j$ (c). The areal coverage is normalized by the areal coverage of reference C_{ref} for a given stick density n and grid resolution l_{avg}/l_q (Fig. S4a). Contour maps obtained by sampling data at l_{avg}/l_q = 1, 2, 4, 8, 16, and 32, and at $\mathcal{P}_q/\mathcal{P}_{eff}$ between 0 and 3 with spacing 0.2.

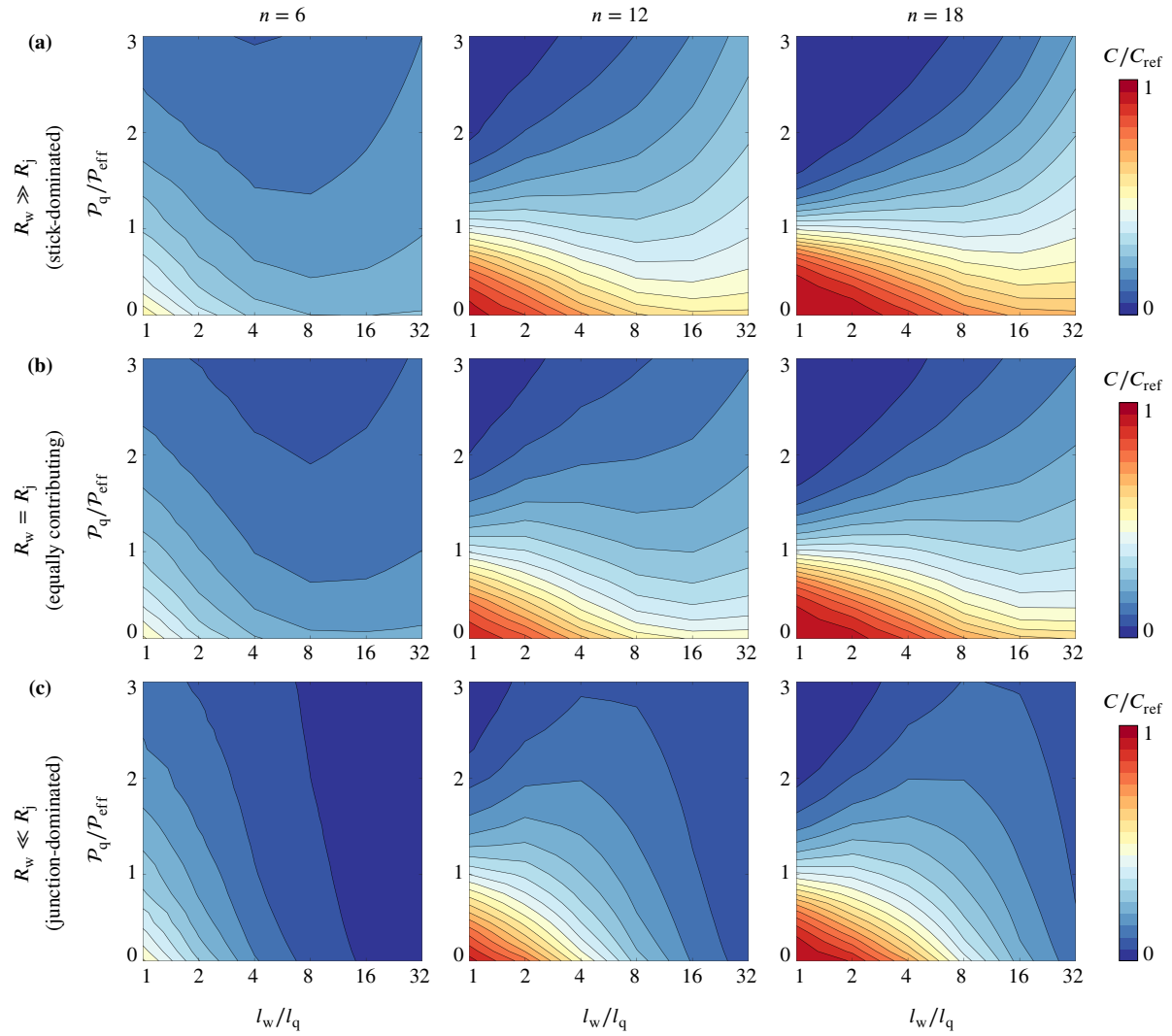

Fig. S6. Areal coverage dependence on grid resolution l_w/l_q and areal power density threshold $\mathcal{P}_q/\mathcal{P}_{eff}$ for numerical geometries. A $\log_2$ scale representation is used for the grid resolution axis. (a,b,c) Contour maps at stick density $n = 6$ (left), 12 (middle), and 18 (right). Results at $n = 12$ (middle) are the same reported in Fig. 3 with label $n = 2\,n_c$ (left). Three resistance scenario are considered: $R_w \gg R_j$ (a), $R_w = R_j$ (b), and $R_w \ll R_j$ (c). The areal coverage is normalized by the areal coverage of reference C_{ref} for a given stick density n and grid resolution l_w/l_q (Fig. 2a). Contour maps obtained by sampling data at $l_w/l_q = 1$, 2, 4, 8, 16, and 32, and at $\mathcal{P}_q/\mathcal{P}_{eff}$ between 0 and 3 with spacing 0.1.

Table S5. Homogeneity quantification: Summary of data presented in Fig. 3e and relative difference between values at different NW content.

homogeneity quantifier	resistance	direction	quantity	A1 or $n = 6$	A2 or $n = 12$	A3 or $n = 18$
electrical tortuosity			values[a]	1.323	1.063	1.001
			relative difference[b]	32.17	6.194	0
$\mathcal{H}$[c] (experimental samples)	$R_w \gg R_j$ (stick-dominated)	x	values	0.9442	0.8741	0.7011
			relative difference[b]	34.66	24.67	0
		y	values	1.007	0.8558	0.7287
			relative difference[b]	38.18	17.44	0
	$R_w = R_j$ (equally contributing)	x	values	0.9374	0.8821	0.7280
			relative difference[b]	28.76	21.17	0
		y	values	0.9709	0.8599	0.7503
			relative difference[b]	29.39	14.60	0
	$R_w \ll R_j$ (junction-dominated)	x	values	0.9494	0.9385	0.8635
			relative difference[b]	9.946	8.694	0
		y	values	0.9791	0.915	0.9089
			relative difference[b]	7.731	0.6729	0
$\mathcal{H}$[d] (numerical samples)	$R_w \gg R_j$ (stick-dominated)		values	1.088	0.8791	0.7231
			relative difference[e]	50.52	21.58	0
	$R_w = R_j$ (equally contributing)		values	1.062	0.8837	0.7566
			relative difference[e]	40.40	16.80	0
	$R_w \ll R_j$ (junction-dominated)		values	1.047	0.9558	0.8830
			relative difference[e]	18.58	8.235	0

[a] Homogeneity quantification performed by Sannicolo et al. [7]. Electrical tortuosity values as provided therein.
[b] Relative difference with respect to the A3 value (of the same set of data) computed as $(|v_{Ai} - v_{A3}|/v_{A3}) \times 100$. The value associated with the Ai-th specimen is indicated with v_{Ai}.
[c] Homogeneity index eqn (S.6) for specimens A1, A2, and A3 from Sannicolo et al. [7] (Fig. S3b).
[d] Homogeneity index eqn (S.6) for numerically generated samples at stick density $n = 6$, 12, and 18. The results are the average of the evaluations performed on 100 realizations for each value of n (65 out of 100 for $n = 6$, the percolated samples).
[e] Relative difference with respect to the $n = 18$ value (of the same set of data).

density threshold $\mathcal{P}_q/\mathcal{P}_{eff}$ and grid resolution l_{avg}/l_q. The figures refer to networks in x- and y-directions, respectively. The results obtained from the numerically generated geometries at $n = 6$, 12, and 18 are provided in Fig. S6 for completeness.

The values of the homogeneity index $\mathcal{H}$ (eqn (S.6)) computed for the experimental geometries (samples A1, A2, and A3) are reported in Table S5 for x- and y-directions and under resistance scenarios $R_w \gg R_j$, $R_w = R_j$, and $R_w \ll R_j$. The values of the homogeneity index $\mathcal{H}$ computed for the numerical geometries at $n = 6$, 12, and 18 are included in the table, but no distinction is made between x- and y-directions because the response of the numerical geometries is, in average, isotropic (as demonstrated in section S2). The values of the electrical tortuosity reported by Sannicolo et al. [7] are included in Table S5 for reference.

References

[1] M. Zhuo, D. Grazioli, A. Simone, Active material utilization and capacity of fiber-based battery electrodes, Electrochimica Acta 333 (2020) 134929. doi:10.1016/j.electacta.2019.134929.

[2] M. Žeželj, I. Stanković, From percolating to dense random stick networks: Conductivity model investigation, Physical Review B 86 (13) (2012) 134202. doi:10.1103/physrevb.86.134202.

[3] Y. Y. Tarasevich, I. V. Vodolazskaya, A. V. Eserkepov, R. K. Akhunzhanov, Electrical conductance of two-dimensional composites with embedded rodlike fillers: An analytical consideration and comparison of two computational approaches, Journal of Applied Physics 125 (13) (2019) 134902. doi:10.1063/1.5092351.

[4] S. Kirkpatrick, Percolation and conduction, Reviews of Modern Physics 45 (4) (1973) 574–588. doi:10.1103/revmodphys.45.574.

[5] O. C. Zienkiewicz, R. L. Taylor, The Finite Element Method. Volume 1: The basis, 5th Edition, Butterworth-Heinemann, 2000.

[6] U. M. Erdem, Fast line segment intersection, accessed 2022-11-04.
URL https://www.mathworks.com/matlabcentral/fileexchange/27205-fast-line-segment-intersection

[7] T. Sannicolo, N. Charvin, L. Flandin, S. Kraus, D. T. Papanastasiou, C. Celle, J.-P. Simonato, D. Muñoz-Rojas, C. Jiménez, D. Bellet, Electrical mapping of silver nanowire networks: A versatile tool for imaging network homogeneity and degradation dynamics during failure, ACS Nano 12 (5) (2018) 4648–4659. doi:10.1021/acsnano.8b01242.

[8] C. Forró, L. Demkó, S. Weydert, J. Vörös, K. Tybrandt, Predictive model for the electrical transport within nanowire networks, ACS Nano 12 (11) (2018) 11080–11087. doi:10.1021/acsnano.8b05406.

[9] S. P. Finner, M. I. Kotsev, M. A. Miller, P. van der Schoot, Continuum percolation of polydisperse rods in quadrupole fields: Theory and simulations, The Journal of Chemical Physics 148 (3) (2018) 034903. doi:10.1063/1.5010979.

[10] J. Li, S.-L. Zhang, Finite-size scaling in stick percolation, Physical Review E 80 (4) (2009) 040104(R). doi:10.1103/physreve.80.040104.

[11] M. Jagota, N. Tansu, Conductivity of nanowire arrays under random and ordered orientation configurations, Scientific Reports 5 (2015) 10219. doi:10.1038/srep10219.

[12] F. Han, T. Maloth, G. Lubineau, R. Yaldiz, A. Tevtia, Computational investigation of the morphology, efficiency, and properties of silver nano wires networks in transparent conductive film, Scientific Reports 8 (2018) 17494. doi:10.1038/s41598-018-35456-7.

[13] D. Kim, J. Nam, Electrical conductivity analysis for networks of conducting rods using a block matrix approach: A case study under junction resistance dominant assumption, The Journal of Physical Chemistry C 124 (1) (2019) 986–996. doi:10.1021/acs.jpcc.9b07163.

[14] D. Kim, J. Nam, Systematic analysis for electrical conductivity of network of conducting rods by Kirchhoff's laws and block matrices, Journal of Applied Physics 124 (21) (2018) 215104. doi:10.1063/1.5051390.

[15] D. Langley, G. Giusti, M. Lagrange, R. Collins, C. Jiménez, Y. Bréchet, D. Bellet, Silver nanowire networks: Physical properties and potential integration in solar cells, Solar Energy Materials and Solar Cells 125 (2014) 318–324. doi:10.1016/j.solmat.2013.09.015.

[16] P. Atkins, J. DePaula, Physical Chemistry, 9th Edition, W. H. Freeman and Company, 2010.

[17] T. Sannicolo, D. Muñoz-Rojas, N. D. Nguyen, S. Moreau, C. Celle, J.-P. Simonato, Y. Bréchet, D. Bellet, Direct imaging of the onset of electrical conduction in silver nanowire networks by infrared thermography: Evidence of geometrical quantized percolation, Nano Letters 16 (11) (2016) 7046–7053. doi:10.1021/acs.nanolett.6b03270.